The International Journal of Advanced Manufacturing Technology
https://doi.org/10.1007/s00170-024-14913-w

ORIGINAL ARTICLE

A submodeling approach for efficient prediction of local temperature profiles in component-scale additive manufacturing

Felix Frölich[1] · Lukas Hof[1] · Clemens Zimmerling[1] · Florian Wittemann[1] · Luise Kärger[1]

Received: 7 October 2024 / Accepted: 6 December 2024

Abstract
To solve the multiscale problem of additive manufacturing of large components by material extrusion (MEX), this work utilizes the methodology of submodeling and shows the necessary modeling steps to apply the methodology to the material extrusion process. The research enables the coupling of high-resolution models and process simulations at the component level. It allows the investigation of local effects such as crystallization effects or the resulting interface strength and its dependence on process variables in critical zones of a component, considering the component geometry as well as global and component-specific process conditions. The principle is verified numerically and validated experimentally, showing good agreement. In addition, different specifications for boundary conditions and submodel sizes are compared and evaluated. Variable time increments are used to apply the submodels with a computational time independent of the component size. In addition, sensitivity analyses provide information on the necessary temporal and spatial discretization of the submodel for the most accurate prediction of the temperature profile.

Keywords Material extrusion (MEX) · Fused filament fabrication (FFF) · Thermal profile · Multiscale · Process simulation · Finite element analysis (FEM)

1 Introduction

Today, additive manufacturing using material extrusion (MEX) is a comparatively innovative process for the production of unreinforced as well as reinforced thermoplastic components and is attracting growing interest within the manufacturing industry. Additive manufacturing is not subject to the limitations of conventional molding tools and complicated multi-step manufacturing processes. In addition, the need for intensive manual labor, expensive production equipment (e.g., tools and autoclaves), and material waste in the production process is significantly reduced. Additive manufacturing of pure thermoplastics [1], but especially of compounds with cut or continuous fiber reinforcements [2, 3], offers high performance and, thanks to the design freedom gained, a promising strength-to-weight ratio of the manufactured components [4].

The mechanical properties of components produced with MEX result not only from the selected trajectory, but also from the resulting geometry of the deposited strands, the interface strength of two deposited strands, and the degree of crystallization within a strand. These local properties are significantly influenced by the thermal history [5–9]. The local temperature profiles depend on several factors determined by the process parameters or the hardware used. The process parameters interact strongly with each other, which makes it difficult to investigate the influencing factors individually, but also makes it clear that understanding this interaction is crucial for the further development of MEX processes.

The influence of the process parameters on the local temperature history and thus on the mechanical properties is usually determined by experiments on printed specimens [10–13]. Due to the large number of process parameters, experimental investigations are very time-intensive [14]. In addition, the measured properties at the coupon level do not necessarily correspond to the actual properties of the printed component. This is because different process con-

✉ Felix Frölich
felix.froelich@kit.edu

[1] Institute of Vehicle System Technology - Lightweight Engineering, Karlsruhe Institute of Technology (KIT), Rintheimer Querallee 2, Karlsruhe 76131, Baden-Württemberg, Germany

Published online: 27 December 2024

ditions may prevail during the component manufacturing [15]. For example, the distance between the deposition of two adjacent strands can deviate. Especially for structures printed with integrated discontinuous and continuous fibers, the interfacial strength and the associated distinct anisotropy is a limiting factor for the resulting strength of the component [16, 17].

Due to the described limitations and difficulties of experimental investigations, an analysis with the help of numerical methods is in high demand. For the investigation of resulting strand geometries, different approaches based on the finite volume method (FVM) [18–22] or the smoothed particle hydrodynamics method (SPH) [23–26] have been developed. Zhang and Chou [27] developed a finite element analysis (FEA) for heat transfer simulation, which used the activation and deactivation of finite elements to map the material deposition process. To investigate the influence of process parameters on the distortion and residual stresses, Favaloro et al. [28] and, further, Brenken et al. [29] developed a simulation approach based on the commercial FE software ABAQUS. This work forms the basis for the method presented in this paper. Ramos et al. [30] propose an FE-based heat transfer model for efficient thermal history prediction. They also use the element activation approach and additionally introduce adaptive coarsening of the elements through an error-based coarsening condition. In addition to these publications, several other studies have been published on FE-based methods for the prediction of temperature profiles [31, 32] or process-induced prediction of distortion and residual stresses [33–35]. Brenken et al. [36] published methods to predict the crystallization that occurs during the printing process of short-fiber reinforced thermoplastics, while Barocio et al. [37] and other authors [7, 31, 38–40] published approaches to predict the bonding that occurs between individual deposited strands. To predict interfacial effects during the manufacturing of a component, Sinha et al. [41] developed a heat transfer simulation method based on the finite difference method to determine thermal interface profiles computationally.

These various publications clearly show that the local effects described above, such as interfacial strength, degree of crystallinity, and strand geometry, are determined by the local temperature profile. To accurately predict these local temperature profiles, a sufficiently fine discretization of the individual strands is required. In addition, the high cooling rates require very small time increments during the simulation compared to the process time. For the process simulation of entire components, such a fine spatial and temporal discretization is hardly feasible, since the very small dimensions of the individual strands compared to the possible component size lead to unmanageable computation times. Therefore, micro- or meso-level methods are used for the numerical investigation of local effects. However, to investigate the influence of the effects on the strength of a component, a prediction of the local effects concerning the process conditions within the component is required. Thus, predicting the mechanical properties within the component is a multiscale problem that requires both fine-resolution models as well as the macro-scale process and component conditions. The research underlying this paper addresses this research gap with the aim of being able to use fine-resolution models at the component level and thus to be able to predict local properties within printed components using these meso- and micro-models.

To deal with similar multiscale problems, the submodeling approach is used in different implementations in other technical areas [42–44]. The submodeling approach follows the SAINT-VENANT principle, according to which the influence of local effects decreases with increasing distance. By implementing this principle for the numerical prediction of certain quantities, information from a macro-simulation is transferred to models with finer resolution. This technique can also be found in approaches to simulate the powder bed fusion process [45]. The applicability of the general method to the MEX process and the process-specific assumptions to be made have not yet been demonstrated. The present paper addresses this research question and applies the general approach of submodeling to the MEX process. The suitability of submodeling for the MEX process is based on the fact that the high cooling rates of the process and the comparatively low thermal conductivity of thermoplastics indicate that cooling effects such as free convection and radiation are mainly responsible for the local temperature profile during MEX. The work presents a methodology that allows the coupling of fine-resolution mesomodels with MEX process simulations at the component level. The information about the local process conditions within the component is derived from an upstream process simulation of the entire component with coarser discretization and transferred to the small, fine-resolution model, the so-called submodel. Different thermal boundary conditions, the size of the submodel, and its discretization, supported by numerical verification and experimental validation, are investigated and discussed. Based on the good validation results, a recommendation is given for the size of the submodel and the boundary conditions.

2 Methodology

2.1 Submodeling concept

The FE software ABAQUS 2023 and its plug-in for modeling additive manufacturing processes are used for simulation. Element activation according to a given trajectory enables the modeling of material extrusion. A predefined initial tem-

perature of an element represents the extrusion temperature. In addition, the plug-in considers continuously changing surfaces with advancing element activation and the associated convection and radiation.

The high cooling rates described in the literature [46] and the comparatively low thermal conductivity of thermoplastics indicate that cooling effects such as free convection and radiation are mainly responsible for the local temperature profile during MEX. This paper presents a method based on the submodeling approach with time-dependent boundary conditions, which allows modeling only a small volume around an area of interest to predict the local temperature profile. This allows a finer spatial and temporal resolution and thus a more accurate representation of the local temperature profile. The fundamental principle behind submodeling is the SAINT- VENANT principle [47], according to which local effects diminish with distance. Thus, the prediction uncertainty should be sufficiently small if boundary conditions and the size of the submodel are defined appropriately.

Figure 1 schematically shows the submodeling approach: To predict the temperature profile at a given point on the component as accurately as possible, only a section is simulated. This section represents the submodel. While the entire component is discretized in a state-of-the-art process simulation and thus represents the domain to be solved, the submodel approach models only a smaller area around the area to be investigated. There are no elements in the region outside the submodel. The submodeling method follows the approach that the modeling of the printing process for the small submodel is, in terms of the printing time and trajectory, the same as for the entire component modeled. The elements within the submodel are thus activated at the same time as the elements would be activated at the corresponding location during the simulation of the entire component. The local process conditions at the domain boundaries of the submodel are derived from an upstream simulation of the entire component with a coarser discretization. Suppose the temperature profile is to be predicted at a point near the component's boundary. In that case, these boundary effects, such as heat exchange with the air or the build platform, are also modeled within the submodel.

2.2 FE process modeling approach and governing equations

The governing equation for thermal modeling is the heat balance equation in combination with the generalized Fourier equation [48]. It can be formulated as the weak form by multiplying a test function δT, integrating over the domain Ω, and applying the chain rule and the divergence theorem:

$$\int_{\Omega} \rho c_{\mathrm{p}} \frac{\partial T}{\partial t} \delta T \, \mathrm{d}V = -\int_{\Omega} (\boldsymbol{\kappa} \nabla T) \cdot (\nabla \delta T) \mathrm{d}V - \int_{\Gamma_O} s \delta T \, \mathrm{d}A, \tag{1}$$

where T is the temperature, t is the time, ρ is the material density, c_{p} is the heat capacity, $\boldsymbol{\kappa}$ is the thermal conductivity tensor, and s is a surface flux at the boundary Γ_O. V stands for the volume, A for the surface, and the nabla operator ∇ expresses the gradient. The domain Ω changes continuously as the printing process progresses, resulting in a continuously changing domain boundary Γ_O. Heat flow source terms such as those caused by crystallization effects are not taken into account here.

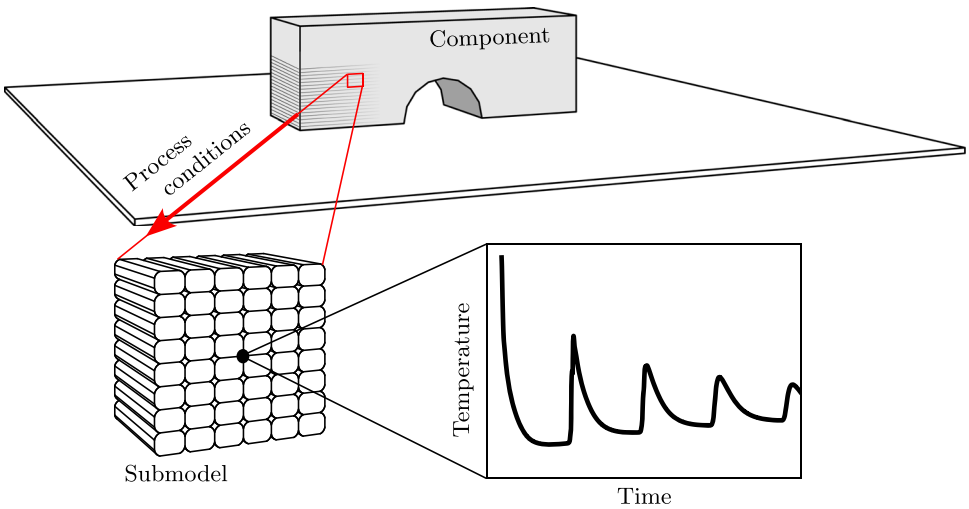

Fig. 1 Schematic representation of the submodel approach: To predict the temperature profile at a certain point on the component as accurately as possible, only a small section is simulated. This section represents the submodel. The local process conditions are derived from an upstream process simulation of the entire component

In a process simulation of the entire component, the heat flow s can be formulated by

$$s = s_{\text{conv}} + s_{\text{rad}} + s_{\text{hp}}. \tag{2}$$

s_{conv} describes the heat flux caused by free convection defined as

$$s_{\text{conv}} = h_{\text{conv}}(T - T_{\text{amb}}), \tag{3}$$

with ambient temperature T_{amb} and the convection coefficient h_{conv}. s_{rad} describes the heat flux by radiation, defined as

$$s_{\text{rad}} = \sigma\epsilon(T^4 - T_{\text{amb}}^4), \tag{4}$$

with Stephan-Boltzmann constant σ and emissivity coefficient ϵ. s_{hp} describes the heat flux into the component due to the heat of the build platform.

The smaller domain Ω_{sub} of the submodel implies a change in the surface flux s. The heat flux into the system through the build platform is not present in the submodel. The convection and radiation of the free surfaces at the printing front within the system are still present. In addition, there is a heat flux $s_{\text{poly}}^{\text{cond}}$ across Γ_O from the submodel into the surrounding printed structure. Thus, the heat flux across Γ_O of the submodel is given by

$$s = s_{\text{conv}} + s_{\text{rad}} + s_{\text{poly}}^{\text{cond}}. \tag{5}$$

2.3 Boundary conditions of the submodel

The geometry of the submodel is defined as a cuboid volume around the area of interest (in this case the center point CP). This allows the boundary conditions to be defined individually for each surface of the submodel. In this work, different boundary conditions to represent the heat flow $s_{\text{poly}}^{\text{cond}}$ over each surface are compared. These methods include adiabatic conditions ($s_{\text{poly}}^{\text{cond}} = 0$), uniform and constant Dirichlet boundary conditions ($T_{\text{poly}}^{\text{const}}$), and uniform and time-dependent Dirichlet boundary conditions ($T_{\text{poly}}(t)$). Figure 2 shows the defined boundary conditions at the domain boundaries at the CP printing time. The left side of the figure shows an additively manufactured cube modeled according to the state-of-the-art. The entire cube represents the domain and is therefore filled with elements. The cooling effects are defined by convection s_{conv} and radiation s_{rad} over all domain boundaries and the resulting free surfaces within the domain. The heat flow through the heated build platform s_{hp} is implemented by a Dirichlet boundary condition. The right side of the figure shows the modeling with the submodeling method. Here, only a certain area around the CP is filled with elements, which represents the model domain. The domain boundaries to the surrounding polymer, where the boundary conditions are defined, are shown in red. Inside the domain, heat flows result from convection s_{conv} and radiation s_{rad} over the free surfaces occurring during the process (shown in blue).

In the actual process, the polymer temperatures $T_{\text{poly}}(t, x, y, z)$ vary with location and time along the submodel boundaries. However, this work aims for the simplest possible submodeling, so these location dependencies of the Dirichlet boundary conditions are ignored. The recommended procedure for determining these conditions involves an upstream process simulation of the entire component, which provides the temperatures for each submodel surface. A coarser discretization can be used for this simulation. The temperatures are determined as shown in Fig. 3 for the y and z surfaces: $T_{\text{poly}}^{\text{y}-}$, $T_{\text{poly}}^{\text{y}+}$, $T_{\text{poly}}^{\text{z}-}$ and $T_{\text{poly}}^{\text{z}+}$. The constant Dirichlet boundary condition $T_{\text{poly}}^{\text{const}}$ is defined as the temperature at the time of printing the layer containing the CP. These temperatures are measured at points marked in Fig. 3, at a distance from the CP equal to half the submodel edge length. The time-dependent Dirichlet boundary condition $T_{\text{poly}}(t)$ is

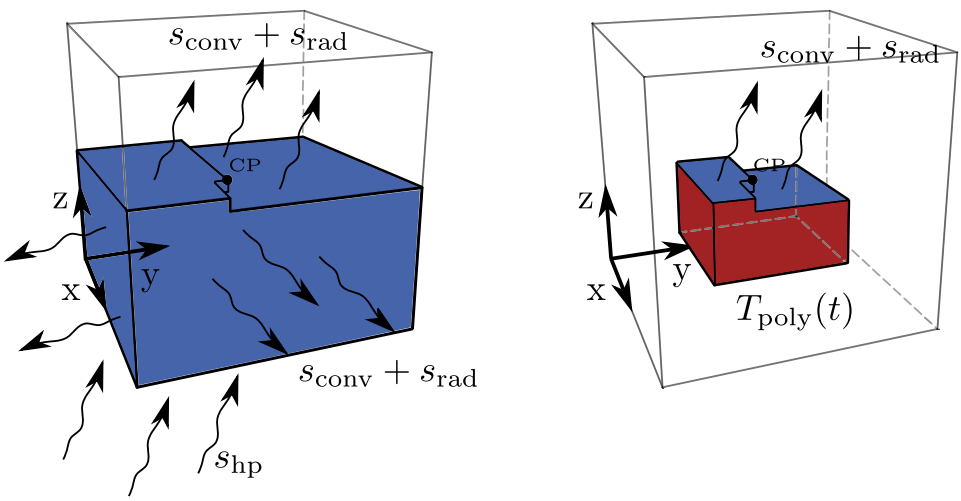

Fig. 2 Schematic representation of the defined boundary conditions for modeling according to the state-of-the-art (left) and with the submodeling method (right)

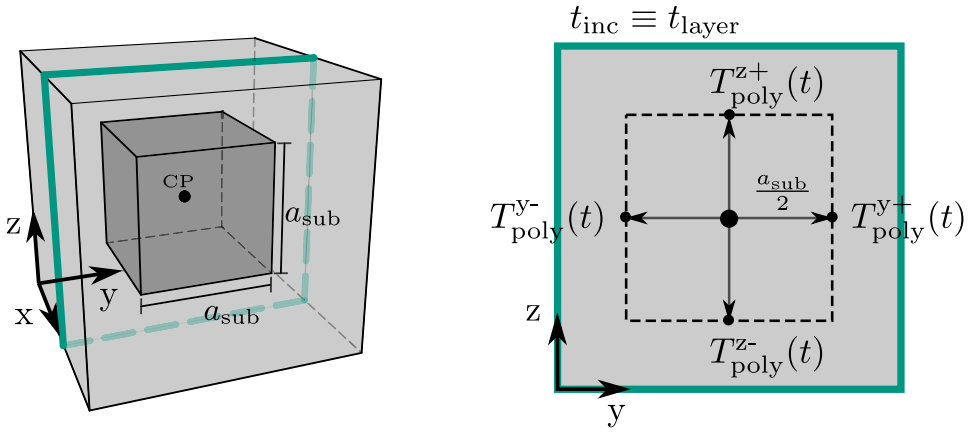

Fig. 3 Schematic representation of the method for determining the time-dependent Dirichlet boundary condition $T_{poly}(t)$ from an upstream process simulation of the entire component with low computational effort

defined as the temperature evolution at these points. For the upstream simulation, a time increment t_{inc} can be chosen so that one complete layer is activated per step. The element height equals the strand height, and the element width equals the strand width s_{width} or a multiple thereof, ensuring that the nodes of the component simulation and the submodel boundary overlap. Linear interpolation between the specified time-dependent temperature values is used for the submodel simulation.

2.4 Time discretization

With the submodeling approach presented here, a high temporal resolution is only required when strands are deposited within the submodel. At times when no elements of the submodel are activated, i.e., other areas of the component are being printed, the heat input into the center is very low and the cooling rates to be recorded are smaller. Therefore, at these times, $t^{out}_{inc} >> t^{sub}_{inc}$ can be selected. A transition region is defined in which no elements of the submodel are activated, but small t^{sub}_{inc} are still defined (marked orange in Fig. 4). This allows the cooling rates immediately after leaving the virtual nozzle of the submodel to be taken into account and a single increment ($n_{t_{inc}} = 1$) to be defined until the nozzle re-enters the submodel. The T_{poly} Dirichlet boundary condition ensures that when the nozzle re-enters the submodel (i.e., elements are reactivated and thermal energy is introduced into the system), the temperature distribution in the real component matches the real process conditions. This makes the required computation time of the new method independent of the size of the entire component.

3 Process and material for method verification and validation

3.1 Process

The *Composer A4* made by *Anisoprint* was used to manufacture the validation components. The nozzle used has a diameter of 0.4 mm. An extrusion width of 0.45 mm is specified in the slicer. The slicer-specific overlap of the individual

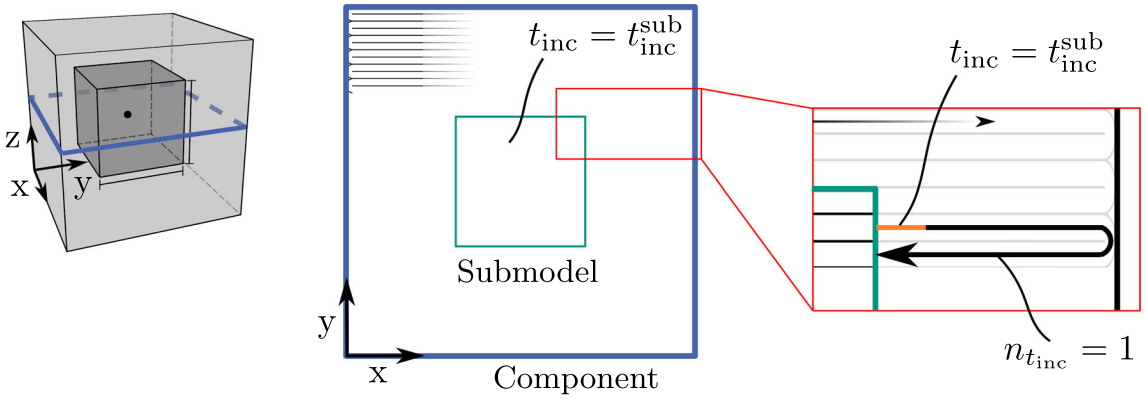

Fig. 4 Illustration of the defined time increment t_{inc} within the submodel (green) with $t_{inc} = t^{sub}_{inc}$ and for the time when the filament would be deposited outside the modeled domain. Here, the t_{inc} for a given time (orange) corresponds to the increment within the submodel $t^{out}_{inc} = t^{sub}_{inc}$. The remaining time (black) is defined by one increment ($n_{t_{inc}} = 1$)

strands, the width of the component, and the trajectory used in this work result in a strand width s_{width} of approximately 0.41 mm, as shown in Table 1. The slicer and printer settings shown in Table 1 were chosen for the experiments as well as the simulations. The fan was switched off, and the build chamber was open due to the need to insert the thermocouples. To measure the room temperature T_{room}, a thermocouple was attached to the build platform so that the measurement point was at the height of the printed component. The average of the five measurements of the room temperature was $T_{\text{room}} = 28.47°C$. The higher temperature compared to the lab temperature is due to radiant heat from the build platform.

3.2 Materials

The material used is BASF Ultrafuse unreinforced PLA filament [49]. The polymer's low melting and glass transition temperatures, low tendency to warp, and relatively high surface hardness make it particularly well suited for additive manufacturing, allowing for robust process control [50]. Due to its good printability, PLA has been exemplarily used in this work.

In this work, the mesostructure is modeled homogenized. The individual strands and the process-typical voids are therefore not explicitly modeled but combined to form a homogenized region. The given material properties thus also represent homogenized values of the process-typical mesostructure: The density $\rho_{\text{PLA}} = 1208\,\text{kg/m}^3$ of the PLA structure produced using the process parameters from Table 1 was measured according to the Archimedean principle using the *ME-DNY-43* density meter and the *ME204T/00* analytical balance from *Mettler Toledo*. The anisotropic thermal conductivity $\boldsymbol{\kappa}$ of the printed structure with unidirectional material orientation is set to $\kappa_x = 0.195\,\text{W/mK}$, $\kappa_y = 0.135\,\text{W/mK}$, and $\kappa_z = 0.181\,\text{W/mK}$ according to Elkholy et al. [51]. The temperature-dependent specific heat capacity $c_{\text{p}}(T)$ was determined using differential scanning calorimetry (DSC) and is shown in Fig. 5. Non-isothermal DSC experiments further show that no significant crystallization effects occur at the cooling rates typically encountered in this process. Therefore, no latent heat is taken into account.

Table 1 Slicer and process parameters selected for the manufacturing of all specimens

Process parameter	Value	Unit
Nozzle temperature T_{N}	212	°C
Bed temperature T_{bed}	55	°C
Layer height l_{height}	0.2	mm
Extrusion width e_{width}	0.45	mm
Strand width s_{width}	0.41	mm
Infill printing speed v_{infill}	50	mm/s

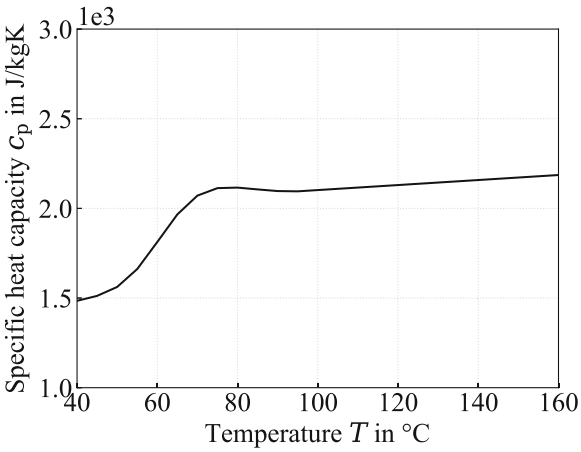

Fig. 5 Temperature-dependent specific heat capacity $c_{\text{p}}(T)$ of the PLA used, measured by DSC

4 Mesh size and time increment

To predict the temperature history as accurately as possible, the mesh size and the selected time increment t_{inc} are crucial. This section therefore presents a sensitivity analysis to identify the required mesh size and t_{inc}. The study includes the accurate prediction of the temperature gradient within a strand as well as the requirement for a steady curve of temperature history.

Mesh size To quantify the required number of elements within a strand not only to the strand width (y-direction) and height (z-direction) but also along the extrusion direction (x-direction), a unit cell is introduced, as shown in Fig. 6. Its width and height are equal to the strand width s_{width} and height a_{height}, and its length in the extrusion direction is equal to s_{width}. This allows a minimum number of elements to be defined for all axes. Figure 6 shows examples of meshing concerning the edge lengths of the unit cell.

To investigate the sensitivity of the element size to the temperature gradient, a single strand deposited on the heated build platform is considered. This represents the extreme case in terms of the temperature gradient. The process parameters listed in Table 1 were used for the simulation studies. As shown in Fig. 7, the temperature profile along the height of the strand (z-direction) as well as the width of the strand (y-direction) at the time of deposition (1) and at the same time 10 mm behind (2) are determined to evaluate the spatial discretization. In the x-direction, the temperature profile along the top of the strand is shown. The t_{inc} was chosen as a function of the element size in the extrusion direction (x-direction), resulting in one element being activated in the x-direction per t_{inc}. Figure 8 shows the percentage deviation of the different discretizations from the finest discretization of 10 elements per edge length of the unit cell, averaged over

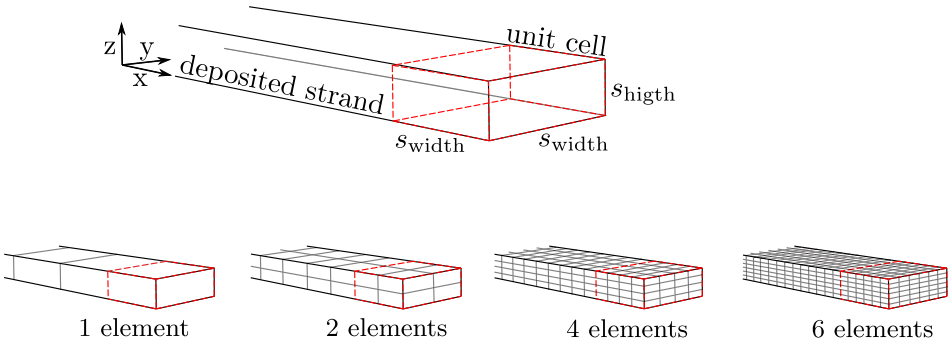

Fig. 6 Introduced unit cell to quantify the required number of elements within a strand in terms of strand width (y-direction), strand height (z-direction), and extrusion direction (x-direction) (top). Below are examples of meshing about the edge length of the unit cell

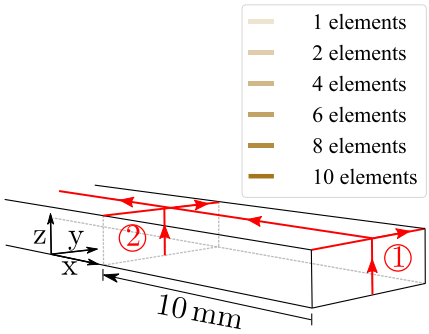

(a)

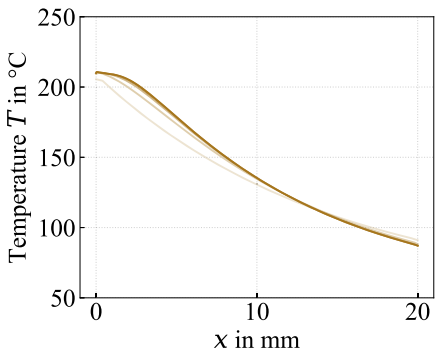

(b) X-direction.

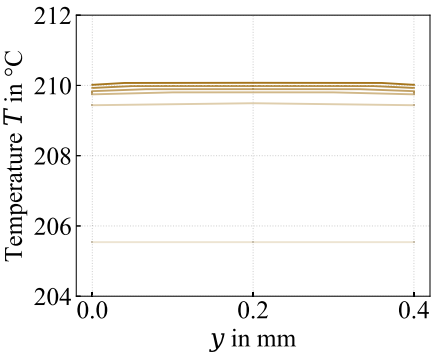

(c) Y-direction at point 1.

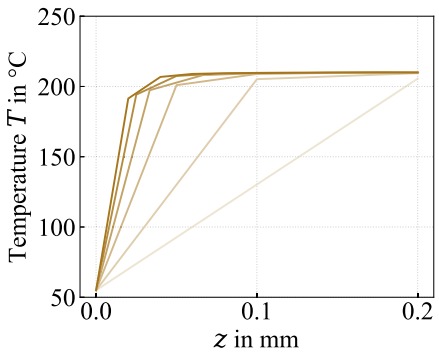

(d) Z-direction at point 1.

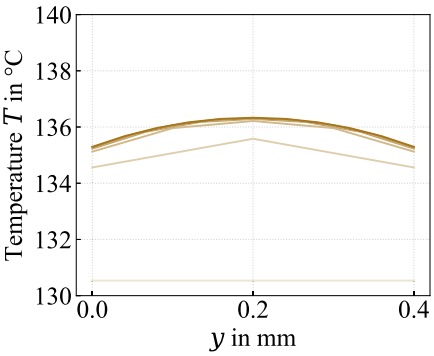

(e) Y-direction at point 2.

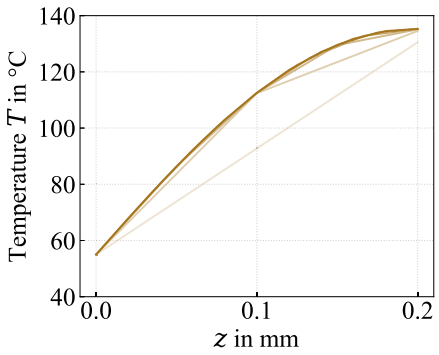

(f) Z-direction at point 2.

Fig. 7 Results of the mesh analysis of the spatial discretization on the temperature distribution within a deposited strand. Performed with 1, 2, 4, 6, 8, and 10 elements per side length of the unit cell and evaluated immediately after element activation (point 1), shown in **c** and **d**, and 10 mm afterward (point 2), shown in **e** and **f**

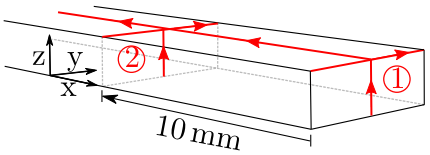

(a)

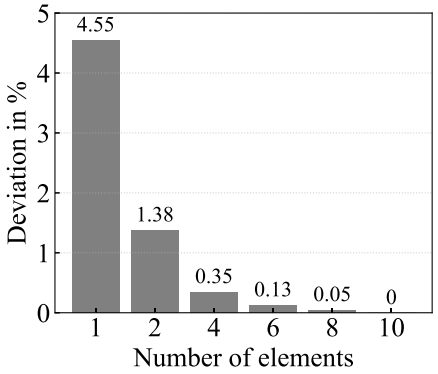

(b) X-direction.

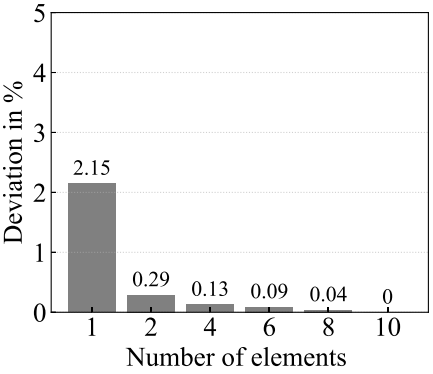

(c) Y-direction at point 1.

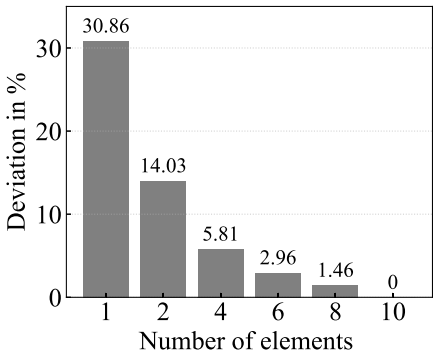

(d) Z-direction at point 1.

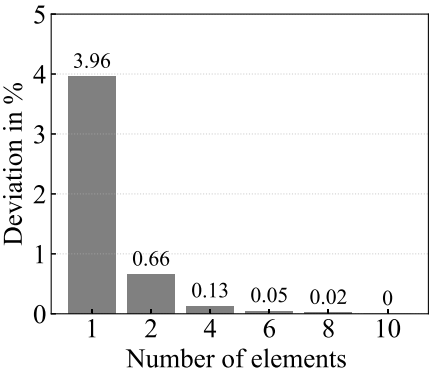

(e) Y-direction at point 2.

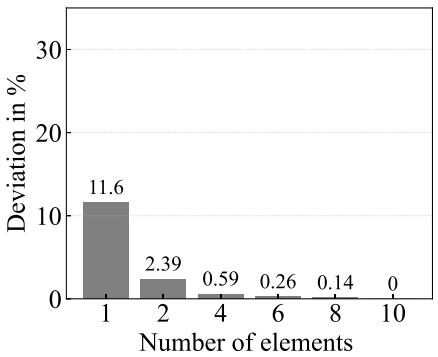

(f) Z-direction at point 2.

Fig. 8 Percentage deviation of the different discretizations concerning the finest discretization of 10 elements per edge length of the unit cell. Averaged over all nodes along the respective path. Performed with 1, 2, 4, 6, 8, and 10 elements and evaluated immediately after element activation (point 1), shown in **c** and **d**, and 10 mm later (point 2), shown in **e** and **f**

all nodes along the respective path. Based on the average deviations, two elements per unit cell along the extrusion direction (x-direction) are considered sufficient. However, at least four elements are required along the height and width of the strand. For the process parameters used in this work, the elements therefore have the edge lengths $l_x = 0.205$ mm, $l_y = 0.1025$ mm, and $l_z = 0.05$ mm.

Time increment To demonstrate the required t_{inc}, four 20 mm strands were placed side by side and on top of each other on a heated build platform. Four elements were selected for each edge of the unit cell. Figure 9 shows the temperature profile in the center of the resulting 2x2 strands component for different t_{inc}. In addition to the t_{inc} that results in the activation of one element along the extrusion direction per t_{inc} (1 element in x-direction), a smaller (1/2 element in x-direction) and a larger t_{inc} (2 elements in x-direction) were selected. Figure 9 b shows that if t_{inc} is selected so that an element row is only activated every second increment, the temperature profile does not show the typical continuous curve. If several element rows are activated per t_{inc}, the temperature

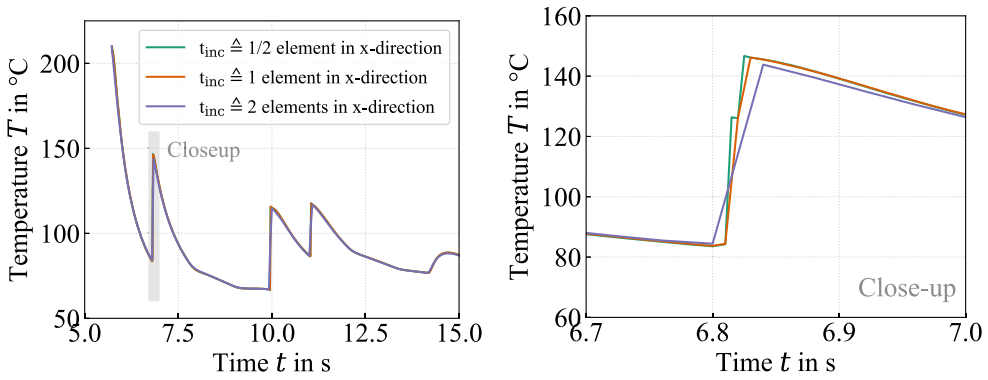

Fig. 9 Temperature profile at a point in the filament from the time of its activation with three different time increments: t_{inc} set to activate two rows of elements per increment ($t_{inc} \widehat{=}$ 2 element in the x-direction), t_{inc} set to activate exactly one row of elements ($t_{inc} \widehat{=}$ 1 element in the x-direction), and t_{inc} set to activate one element every second increment ($t_{inc} \widehat{=}$ 1/2 element in the x-direction) (**a**). Close-up for a more detailed comparison of cooling rates and temperature (**b**)

peak is slightly underestimated. However, the analysis shows that such larger time increments can also be selected for an accurate representation of the temperature profile. Since this work focuses on the most accurate representation of the history, a t_{inc} is selected as dependent on the element size along the extrusion direction so that one element row is activated per increment and thus the continuous extrusion process is mapped as realistically as possible.

5 Verification of the numerical principle and the submodel size

5.1 Model Setup

To verify the numerical principle, a heat transfer analysis of the additive manufacturing of a cube, as introduced in Section 2, is performed as a generic component. A unidirectional trajectory as shown in Fig. 10 is used.

A cuboid-like submodel as shown in Fig. 2 is modeled around the center point (CP) of the component. The error can be estimated by comparing the temperature curves in the CP. Models with different edge lengths and corresponding boundary conditions are compared to evaluate the necessary size of the modeled volume of the submodel.

The small dimensions of the component allow a temporal and spatial discretization as in the submodel according to the sensitivity analysis presented in Section 4. This ensures that the temperature profile is predicted as accurately as possible, even in the state-of-the-art simulation of the actual component. In this way, the novel submodeling approach can be verified numerically. The process parameters used for the simulation can be found in Table 1. The convection coefficient is set to $h_{conv} = 8\,\mathrm{W/m^2K}$, and the emissivity coefficient is set to $\epsilon = 0.97$ according to [52]. Linear isoparametric 3D elements with 8 heat transfer nodes (DC3D8) are used.

5.2 Temperature prediction accuracy

Figure 11 shows the calculated temperatures T(t) at the CP for both the fine-mesh process simulation (gray) and the submodel with twelve times the extrusion width (4.88 mm) as length under different boundary conditions. The adiabatic boundary condition results in the green curve, the constant Dirichlet boundary condition in the blue curve, and the time-dependent Dirichlet boundary condition in the red curve. Temperature fluctuations are due to renewed heat input from nearby deposited strands. The lower part of Fig. 11 shows the temperature deviations ΔT at the CP over time. The adiabatic boundary condition significantly overestimates the temperature, as no heat can dissipate beyond the submodel's boundaries. The Dirichlet boundary conditions predict the temperature similarly to the simulation of the entire cube, especially immediately after the CP is printed. The constant Dirichlet boundary condition overestimates the temperature for the later process stage. This is because the surface of the submodel cool down during the process after printing the CP, which the constant boundary condition does not account for as opposed to the time-dependent one. The initial overestimation of the temperature and the subsequent underestimation of T when using time-dependent Dirichlet boundary conditions is due to their uniformity.The boundaries of the submodel, extruded before the activation time of the CP, actually have lower temperatures than specified by the selected boundary conditions. The temperatures inside the submodel are

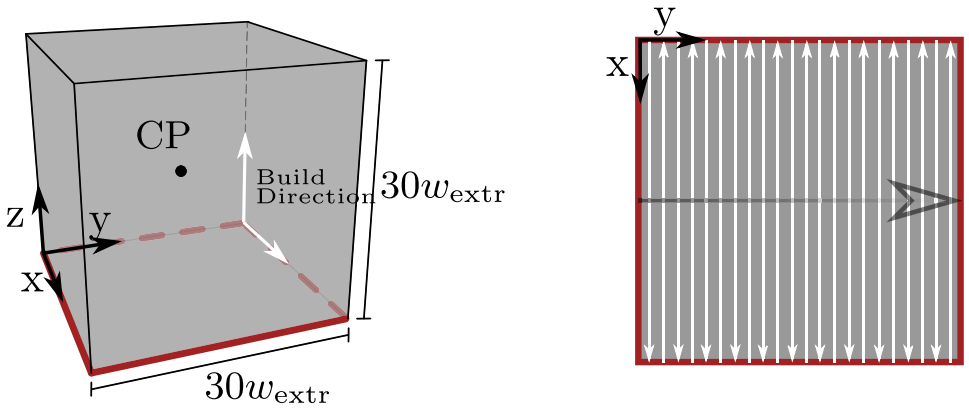

Fig. 10 Cube as a generic component, with edge lengths (left) and the orientation of the unidirectional trajectory (right)

therefore overestimated immediately after extrusion. The reverse effect at the later printed domain boundaries leads to an increasing underestimation of the temperature since a location-dependent consideration of the Dirichlet boundary conditions would predict higher temperatures. However, the error does not grow infinitely but is limited by the choice of the Dirichlet boundary conditions Tpoly(t). The time-dependent Dirichlet boundary condition provides the most accurate temperature curve and is recommended and used to validate the method.

Figure 12 shows the ΔT of submodels of different sizes with time-dependent Dirichlet boundary conditions compared to the state-of-the-art simulation. On average, the initial overestimation and subsequent underestimation of the temperature described above can be seen for all sizes. In addition, the deviations increasingly fluctuate around the mean for smaller submodel sizes. This is due to the increasing negative influence of the chosen boundary conditions on the cooling rate and the resulting temperature peaks in the CP.

The comparison of the computation time between the entire cube and the submodel with the upstream coarser simulation shows that the submodeling approach achieves a reduction of more than 98 %. All simulations were performed on 16 cores. The time advantage increases with larger components, since the required computation time of the submodel is independent of the component size.

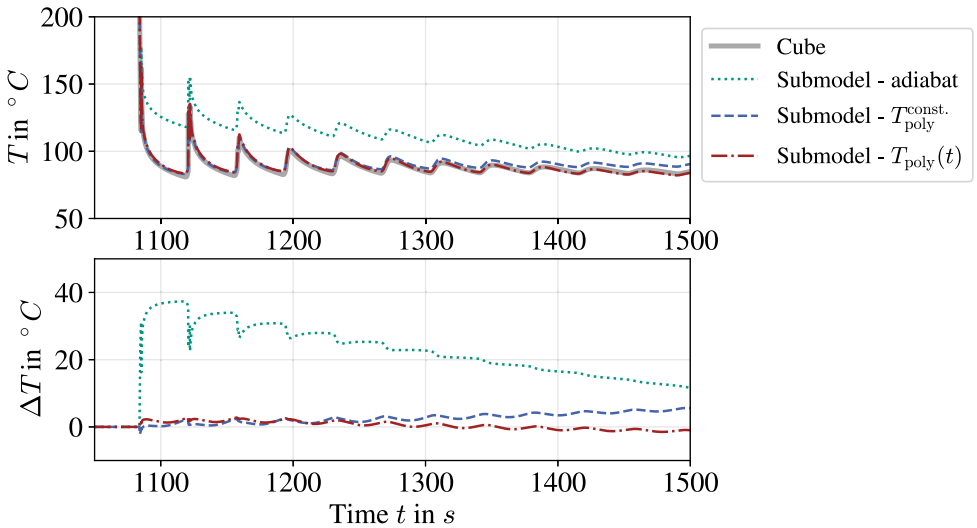

Fig. 11 Calculated temperatures $T(t)$ at the CP of the state-of-the-art process simulation (cube) and the submodel with an edge length of 4.8 mm and different boundary conditions at its surfaces: Adiabatic boundary condition in green, constant Dirichlet boundary condition $T_{\text{poly}}^{\text{const.}}$ in blue, and time-dependent boundary condition $T_{\text{poly}}(t)$ in red. The lower part shows the deviation of the submodel temperatures ΔT from the calculated temperature curve

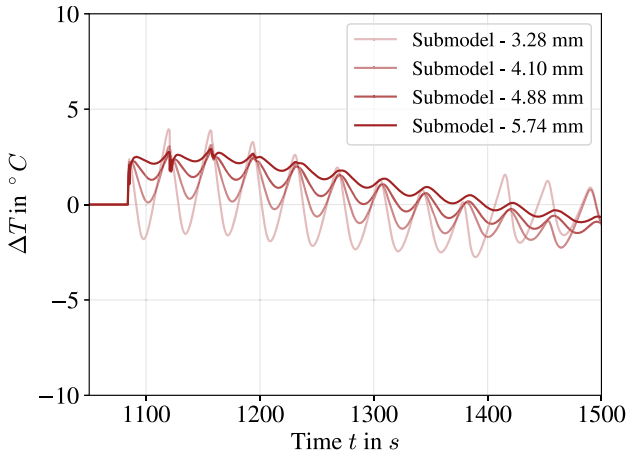

Fig. 12 ΔT of submodels of different sizes

6 Experimental validation

6.1 Experiment

For experimental validation, the temperature profile during the printing of a component was measured using Type K thermocouple sensors with a diameter of 0.07 mm. Due to the small size of the deposited strands, the exact placement of these sensors strongly influences the error of the measurements. Therefore, a component geometry was chosen that minimizes the sources of error. The selected geometry with the indicated trajectory is shown in Fig. 13. To place the sensors, channels with the height of a layer were provided. This allows the sensor to be placed in the same position as reproducibly as possible and the nozzle to be moved over the sensor without displacing the thermocouple. The channel is in the layer with the CP. After printing the layer, the process is interrupted for 30 s to insert and fix the thermocouple. When printing is resumed, temperature recording begins and is evaluated from the first overprint of the sensor. From this point on, the simulation data are compared to the experimental data for validation. The extrusion direction is along the x-coordinate. An additional channel was integrated on the underside of the component to measure the temperature at the point of contact between the component and the build platform. The ambient temperature T_{amb} was measured during the process using a sensor in an area above the build platform at the height of the component. The process parameters given in Table 1 were used, and five measurements were taken. Figure 14 shows the mean values of the measurements at the middle point and the bottom of the component with the corresponding minimum and maximum values.

The heat input from the deposited strands and the rapid cooling can be seen. This results in the expected temperature peaks. In Fig. 14, a temperature peak represents a printed layer. The general increase in the mean temperature at the

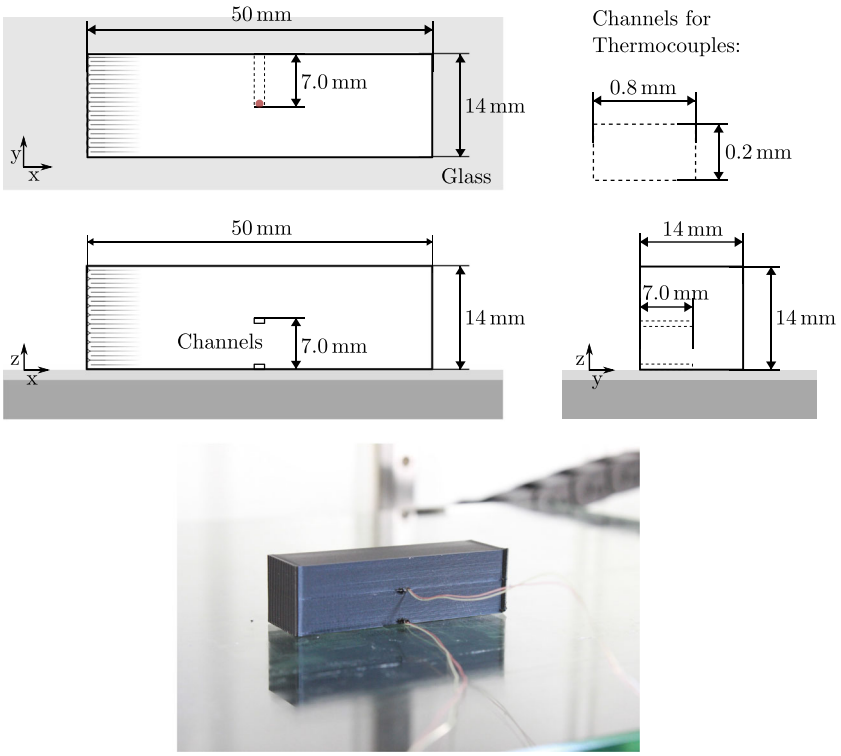

Fig. 13 Component geometry and print setup for experimental validation with thermocouple sensors. The temperature measuring point is marked in red

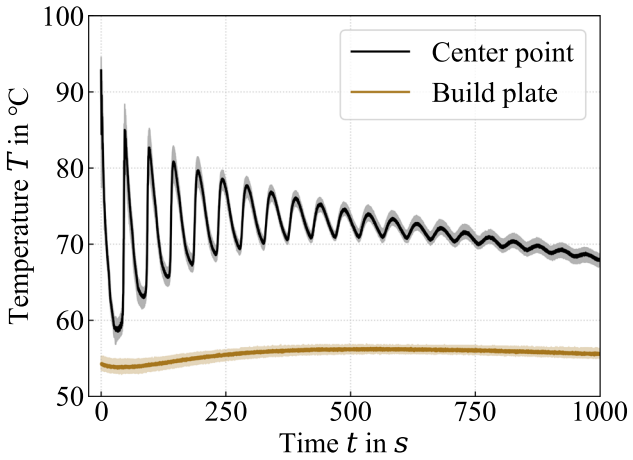

Fig. 14 Mean value of the measured temperature profiles in the center (black) and at the bottom (brown) of the component with the corresponding minimum and maximum (lighter color) value for experimental validation

beginning of the measurement is due to the following phenomenon: The component cools down when the sensor is inserted before the start of the measurement because printing is briefly interrupted during this time. As a result, the temperature in the component is lower at the start of the measurement than it would be during continuous printing. The heat input from the strand deposition after sensor insertion heats the component as a whole. As a result, the temperature in the entire component rises again after the sensor is inserted and the measurement begins. This effect diminishes toward the end of the measurement as the heat input moves away from the measurement point. The temperature profile at the bottom of the component shows no temperature peaks due to the deposition of the strands in the center of the component. This proves that the local cooling rates at the measurement point are predominantly by the cooling effect of convection and radiation and not by heat conduction into the component.

6.2 Process simulation model

For experimental validation, a submodel was modeled around the center of the validation component in Fig. 13. Figure 15 shows the submodel inside the component. Ten times the extrusion width w_{extr} was chosen as the edge length of the submodel. As shown in Fig. 12, this dimension leads to a similar peak temperature prediction as the larger submodels. The model was discretized according to the results of the analysis described in Section 4 with four elements in the strand height and width and two elements per unit length in the extrusion direction. The time increment at a print velocity of $v_{\text{p}} = 50$ mm/s is $t_{\text{inc}} = 0.00412$ s. The time-dependent Dirichlet boundary conditions at the interfaces are derived from the results of the process simulation of the entire component as described in Section 2.3 with $t_{\text{inc}} = t_{\text{layer}}$. The element height was set to the layer height of 0.2 mm. The process parameters from Table 1 were selected. The GCode of the validation component was converted into the real nozzle motion as input for ABAQUS using the open-source software PYGCODEDECODE [53]. This software considers the influence of firmware and hardware limitations on the final nozzle motion, thus enabling an accurate representation of the realistic temperature profiles.

6.3 Comparison of the local temperature profiles

Figure 16a shows the experimentally determined temperature profile in the CP and the temperature profile predicted using the submodeling approach over the same period. The temperature curve is presented starting from the point at which the CP is overprinted, as the thermocouple is capable of detecting temperature only from this moment onwards as described in Section 6.1. Therefore, when comparing simulated and experimental data, the temperature does not start above the melting temperature, but below it. However, it should be noted that in the simulation, temperature mapping is possible

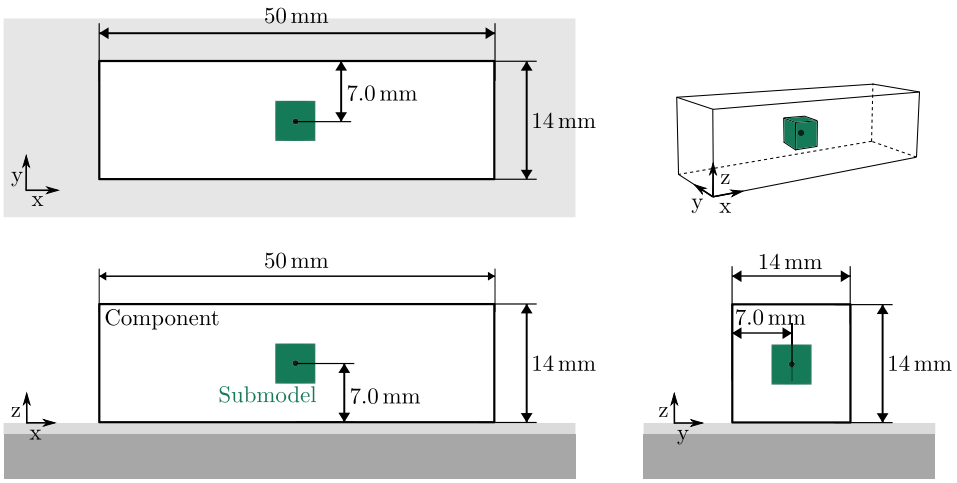

Fig. 15 Schematic representation of the validation component with integrated submodel in green and the measuring point in black

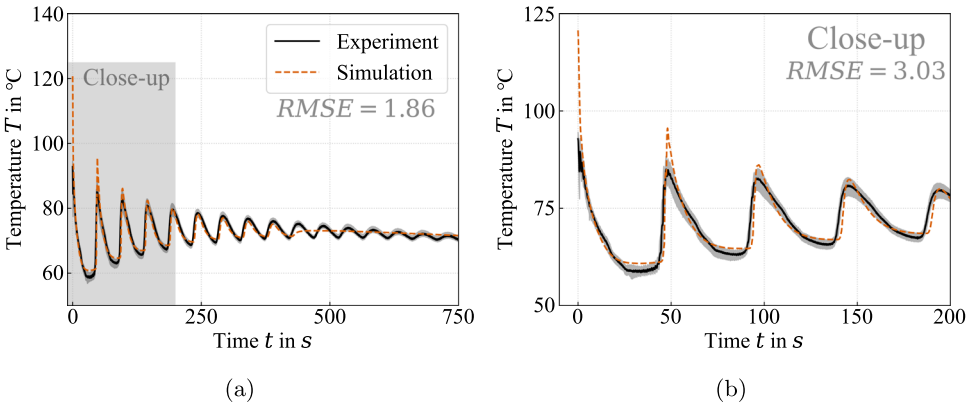

Fig. 16 Temperature curves determined with the novel submodeling method presented in this work and measured with thermocouples sensors in experiments (**a**). Close-up for a more detailed comparison of cooling rates and temperature (**b**). The root-mean-square error (*RMSE*) is given for both sections (**a**) and (**b**)

from the time the CP is printed ("activated" in the simulation). In this case, temperatures in the range of the nozzle temperature are predicted.

Using the submodeling approach, the fine-resolution model can reproduce the measured cooling rates and temperature peaks. Only the two initial temperature peaks are higher in the numerically calculated curve. There are two conceivable reasons for this: First, the nozzle temperature set in the slicer is assumed to be the extrusion temperature in the simulation. However, it is known from the literature [54, 55] that the actual extrusion temperature can differ from the set temperature. On the other hand, due to the thermal inertia of the thermocouple and its limited sampling rate in combination with the comparatively high nozzle speed, the initial temperature peaks may not be recorded as they occur in the process. The constant temperature profile later in the process (after about 400 s) can be explained by the size of the submodel. At the transition from the oscillating to the constant temperature profile, the submodel is already completely printed. This means that no new elements are activated in the submodel domain and therefore no additional heat is added. Overall, however, it can be concluded that the submodeling approach is capable of simulating the temperature history at local points of interest, using finely resolved models locally and accounting for components' geometry and process conditions globally. This is also confirmed by the corresponding root mean square error (*RMSE*). In the time range $t = 0\,\text{s} - 750\,\text{s}$, the $RMSE = 1.86°\text{C}$. In the close-up time range, where local variables such as degree of crystallization and interface strength are significantly influenced, the error is $RMSE = 3.03°\text{C}$.

7 Conclusion

A modeling method based on the submodeling approach is presented, which enables the coupling of high-resolution models and MEX process simulations at the component level. It thus allows the investigation of local effects and their dependence on process variables at local points of interest in a component, taking into account the component geometry as well as global and component-specific process conditions. The submodeling approach follows the SAINT-VENANT principle, according to which local effects decrease with increasing distance. The application of submodeling to the MEX process is based on the fact described in the literature that the high cooling rates typical for the process and the comparatively low thermal conductivity of thermoplastics indicate that cooling effects such as free convection and radiation are mainly responsible for the local temperature profile during MEX. The local process conditions in the investigated component are taken into account by time-dependent Dirichlet boundary conditions, which are determined by an upstream efficient simulation of the entire component in low resolution. In this way, the real process conditions are transferred to the submodel and enable a local prediction of the temperature profile in additively manufactured components during production. The predicted local temperature profile allows accurate prediction of local effects such as interface strength and degree of crystallinity in the component. The work thus provides a modeling approach for the multiscale problem prevalent in MEX.

The required computation time is independent of the component size, which allows an efficient prediction of the temperature history. The numerical principle is verified using a state-of-the-art process simulation on the component level for unidirectional trajectories. Furthermore, different boundary conditions and domain sizes of the submodel are compared and discussed. A sensitivity analysis provides the necessary temporal and spatial discretization for the fine-resolution model used. The presented submodeling method is validated using experimental temperature curves. The validation tests were performed with a commercial fused filament

fabrication printer and unreinforced polylactic acid (PLA). The validation shows a good agreement between the temperature profiles calculated with the submodeling approach and the experimentally determined profiles. The cooling rates and the time sequence of the temperature peaks are in good agreement. The validation shows only slightly higher temperatures in the numerical determination for the first temperature peaks. This is most probably due to a lower effective extrusion temperature compared to the nominal nozzle temperature specified in the slicer and assumed in the simulation, the thermal inertia of the thermocouples, or the limited sampling rate of the sensors. These assumptions need to be investigated in subsequent work to further substantiate the prediction accuracy of the fine-resolution models and their use to predict local crystallinity and interfacial strength of adjacent strands. The work shows that a cuboid model with an edge length of ten times the extrusion width is sufficient for the extrusion of PLA. Similar sizes are expected for other non-reinforced thermoplastics due to their low thermal conductivity. For fiber-reinforced material systems, future work will be needed to determine the required size through investigations such as those described in this article.

Acknowledgements The project in which the presented work has been initiated was funded by the EXU measure KIT Future Fields Project Hybrid^2-PaM. The authors also thank Baden-Württemberg State Ministry of Science, Research and the Arts (MWK) for funding the subsequent project "Basics of a remanufacturing process chain for functional, hybridized polymer components to increase reusability and optimize resource utilization (Restore)" as part of the InnovationCampus Future Mobility (ICM), and the German Research Foundation (DFG) for funding Prof. Kärger's Heisenberg Professorship (project no. 455807141).

Author Contributions Felix Frölich: conceptualization, data curation, formal analysis, investigation, methodology, software, validation, visualization, writing—original draft; Lukas Hof: data curation, investigation, validation, writing—review and editing; Clemens Zimmerling: investigation, methodology, writing—review and editing; Florian Wittemann: investigation, methodology, writing—review and editing, supervision; Luise Kärger: conceptualization, funding acquisition, writing—review and editing, supervision

Funding Open Access funding enabled and organized by Projekt DEAL. This research was supported by the German Research Foundation (DFG), the Baden-Württemberg State Ministry of Science, Research and the Arts (MWK), and the EXU measure KIT Future Fields.

Data Availability The data generated in the context of this work are available from the corresponding authors upon reasoned request.

Declarations

Conflict of interest The authors declare no competing interests.

Ethics approval Authors approve to follow the Ethical Responsibilities of Authors for this journal.

Consent to participate All authors read the final manuscript.

Consent for publication All authors approved the publication of the final manuscript.

Competing interests: The authors declare no competing interests.

References

1. Klippstein H, De Cerio Diaz, Sanchez A, Hassanin H, Zweiri Y, Seneviratne L (2018) Fused deposition modeling for unmanned aerial vehicles (UAVs): a review. Adv Eng Mater 20(2). https://doi.org/10.1002/adem.201700552
2. Blok LG, Longana ML, Yu H, Woods BKS (2018) An investigation into 3D printing of fibre reinforced thermoplastic composites. Add Manuf 22:176–186. https://doi.org/10.1016/j.addma.2018.04.039
3. Lewicki JP, Rodriguez JN, Zhu C, Worsley MA, Wu AS, Kanarska Y, Horn JD, Duoss EB, Ortega JM, Elmer W, Hensleigh R, Fellini RA, King MJ (2017) 3D-Printing of Meso-structurally Ordered Carbon Fiber/Polymer Composites with Unprecedented Orthotropic Physical Properties. Sci Rep 7:1–14. https://doi.org/10.1038/srep43401
4. Compton BG, Lewis JA (2014) 3D-printing of lightweight cellular composites. Adv Mater 26(34):5930–5935. https://doi.org/10.1002/adma.201401804
5. Abbott AC, Tandon GP, Bradford RL, Koerner H, Baur JW (2018) Process-structure-property effects on ABS bond strength in fused filament fabrication. Add Manuf 19:29–38. https://doi.org/10.1016/j.addma.2017.11.002
6. Ammar S, Ben Fraj B, Hentati H, Saouab A, Ben Amar M, Haddar M (2024) Mechanical performances of printed carbon fiber-reinforced PLA and PETG composites. Proc Inst Mech Eng Pt L J Mater Des Appl 238(8):1488–1499. https://doi.org/10.1177/14644207231225761
7. Coogan TJ, Kazmer DO (2017) Healing simulation for bond strength prediction of FDM. Rapid Prototyp J 23(3):551–561. https://doi.org/10.1108/RPJ-03-2016-0051
8. Dey A, Yodo N (2019) A systematic survey of FDM process parameter optimization and their influence on part characteristics. J Manuf Mater Process 3(3). https://doi.org/10.3390/jmmp3030064
9. Sun Q, Rizvi GM, Bellehumeur CT, Gu P (2008) Effect of processing conditions on the bonding quality of FDM polymer filaments. Rapid Prototyp J 14(2):72–80. https://doi.org/10.1108/13552540810862028
10. Ahn SH, Montero M, Odell D, Roundy S, Wright PK (2002) Anisotropic material properties of fused deposition modeling ABS. Rapid Prototyp J 8(4):248–257. https://doi.org/10.1108/13552540210441166

11. Bellini A, Güçeri S (2003) Mechanical characterization of parts fabricated using fused deposition modeling. Rapid Prototyp J 9(4):252–264. https://doi.org/10.1108/13552540310489631
12. Rodríguez-Panes A, Claver J, Camacho AM (2018) The influence of manufacturing parameters on the mechanical behaviour of PLA and ABS pieces manufactured by FDM: a comparative analysis. Materials 11(8). https://doi.org/10.3390/ma11081333
13. Sood AK, Ohdar RK, Mahapatra SS (2010) Parametric appraisal of mechanical property of fused deposition modelling processed parts. Mater Des 31(1):287–295. https://doi.org/10.1016/j.matdes.2009.06.016
14. Kechagias JD, Vidakis N, Petousis M, Mountakis N (2022) A multi-parametric process evaluation of the mechanical response of PLA in FFF 3D printing. Mater Manuf Process 1–13. https://doi.org/10.1080/10426914.2022.2089895
15. Frölich F, Bechtloff L, Scheuring BM, Heuer AL, Wittemann F, Kärger L, Liebig WV (2024) Evaluation of mechanical properties characterization of additively manufactured components. Prog Addit Manuf https://doi.org/10.1007/s40964-024-00700-2
16. Allouch M, Ben Fraj B, Dhouioui M, Kesssentini A, Hentati H, Wali M, Ferhi M (2024) Mechanical, microstructural and numerical investigations of 3D printed carbon fiber reinforced PEEK. Proc Inst Mech Eng C J Mech Eng Sci 238(6):2131–2139. https://doi.org/10.1177/09544062231190534
17. Fan C, Shan Z, Zou G, Zhan L, Yan D (2021) Interfacial bonding mechanism and mechanical performance of continuous fiber reinforced composites in additive manufacturing. Chin J Mech Eng (Eng Ed) 34(1). https://doi.org/10.1186/s10033-021-00538-7
18. Xia H, Lu J, Dabiri S, Tryggvason G (2018) Fully resolved numerical simulations of fused deposition modeling. Part I: fluid flow. Rapid Prototyp J 24(2):463–476. https://doi.org/10.1108/RPJ-12-2016-0217
19. Xia H, Lu J, Tryggvason G (2019) A numerical study of the effect of viscoelastic stresses in fused filament fabrication. Comput Methods Appl Mech Eng 346:242–259. https://doi.org/10.1016/j.cma.2018.11.031
20. Xia H, Lu J, Tryggvason G (2019) Simulations of fused filament fabrication using a front tracking method. Int J Heat Mass Transfer 138:1310–1319. https://doi.org/10.1016/j.ijheatmasstransfer.2019.04.132
21. Mishra AA, Momin A, Strano M, Rane K (2022) Implementation of viscosity and density models for improved numerical analysis of melt flow dynamics in the nozzle during extrusion-based additive manufacturing. Progress Add Manuf 7(1):41–54. https://doi.org/10.1007/s40964-021-00208-z
22. Serdeczny MP, Comminal R, Pedersen DB, Spangenberg J (2019) Numerical simulations of the mesostructure formation in material extrusion additive manufacturing. Add Manuf 28:419–429. https://doi.org/10.1016/j.addma.2019.05.024
23. Bertevas E, Férec J, Khoo BC, Ausias G, Phan-Thien N (2018) Smoothed particle hydrodynamics (SPH) modeling of fiber orientation in a 3D printing process. Phys Fluid 30(10). https://doi.org/10.1063/1.5047088
24. Makino M, Fukuzawa D, Murashima T, Kawakami M, Furukawa H (2017) Analysis of deposition modeling by particle method simulation. Microsyst Technol 23(5):1177–1181. https://doi.org/10.1007/s00542-016-3047-4
25. Ouyang Z, Bertevas E, Wang D, Khoo BC, Férec J, Ausias G, Phan-Thien N (2020) A smoothed particle hydrodynamics study of a non-isothermal and thermally anisotropic fused deposition modeling process for a fiber-filled composite. Phys Fluids 32(5). https://doi.org/10.1063/5.0004527
26. Yang D, Wu K, Wan L, Sheng Y (2017) A particle element approach for modelling the 3D printing process of fibre reinforced polymer composites. Journal of Manufacturing and Materials Processing. 1(1):10. https://doi.org/10.3390/jmmp1010010
27. Zhang Y, Chou Y (2006) Three-dimensional finite element analysis simulations of the fused deposition modelling process. Proc Inst Mech Eng Pt B J Eng Manufact 220(10):1663–1671. https://doi.org/10.1243/09544054 JEM572
28. Favaloro AJ, Barocio E, Brenken B, Pipes RB, Barocio E, Pipes RB (2017) Simulation of polymeric composites additive manufacturing using Abaqus. Dassault Systemes' Science in the Age of Experience. pp 103–114
29. Brenken B, Barocio E, Favaloro A, Kunc V, Pipes RB (2019) Development and validation of extrusion deposition additive manufacturing process simulations. Add Manuf 25:218–226. https://doi.org/10.1016/j.addma.2018.10.041
30. Ramos N, Mittermeier C, Kiendl J (2023) Efficient simulation of the heat transfer in fused filament fabrication. J Manuf Process 94:550–563. https://doi.org/10.1016/j.jmapro.2023.03.030
31. Roy M, Yavari R, Zhou C, Wodo O, Rao P (2019) Prediction and experimental validation of part thermal history in the fused filament fabrication additive manufacturing process. J Manuf Sci Eng Trans ASME 141(12). https://doi.org/10.1115/1.4045056
32. Zhou Y, Nyberg T, Xiong G, Liu D (2016) Temperature analysis in the fused deposition modeling process. Proceedings - 2016 3rd International Conference on Information Science and Control Engineering, ICISCE 2016. pp 678–682 https://doi.org/10.1109/ICISCE.2016.150
33. Zhou Y, Lu H, Wang G, Wang J, Li W (2020) Voxelization modelling based finite element simulation and process parameter optimization for fused filament fabrication. Mater Design 187:108409. https://doi.org/10.1016/j.matdes.2019.108409
34. Nickel AH, Barnett DM, Prinz FB (2001) Thermal stresses and deposition patterns in layered manufacturing. Mater Sci Eng, A 317(1–2):59–64. https://doi.org/10.1016/S0921-5093(01)01179-0
35. Trofimov A, Le Pavic J, Pautard S, Therriault D, Lévesque M (2022) Experimentally validated modeling of the temperature distribution and the distortion during the Fused Filament Fabrication process. Add Manuf 54:102693. https://doi.org/10.1016/j.addma.2022.102693
36. Brenken B, Favaloro A, Barocio E, DeNardo NM, Pipes RB (2016) Development of a model to predict temperature history and crystallization behavior of 3d printed parts made from fiber-reinforced thermoplastic polymers. Int SAMPE Tech Conf 2016 –January
37. Barocio E, Brenken B, Favaloro A, Pipes RB (2022) Interlayer fusion bonding of semi-crystalline polymer composites in extrusion deposition additive manufacturing. Comp Sci Technol 230:109334. https://doi.org/10.1016/j.compscitech.2022.109334
38. Thomas JP, Rodriguez JF (2000) Modeling the fracture strength between fused-deposition extruded roads. Nucl Phys 1
39. Bellehumeur C, Li L, Sun Q, Gu P (2004) Modeling of bond formation between polymer filaments in the fused deposition modeling process. J Manuf Process 6(2):170–178. https://doi.org/10.1016/S1526-6125(04)70071-7
40. Lepoivre A, Boyard N, Levy A, Sobotka V (2022) Methodology to assess interlayer quality in the material extrusion process: a temperature and adhesion prediction on a high performance polymer. Add Manuf 60. https://doi.org/10.1016/j.addma.2022.103167
41. Sinha S, Lynch SP, Meisel NA (2021) Heat transfer simulation of material extrusion additive manufacturing to predict weld strength between layers. Add Manuf 46:102117. https://doi.org/10.1016/j.addma.2021.102117
42. Stoyanov S, Dabek A, Bailey C (2013) Thermo-mechanical submodelling of BGA components in PCB reflow. In: Proceedings of the 36th International Spring Seminar on Electronics Technology. pp 253–258. https://doi.org/10.1109/ISSE.2013.6648252
43. Ganesan VV, Jain A (2021) Computationally-efficient thermal simulations of large Li-ion battery packs using submodeling technique.

Int J Heat Mass Transfer 165:120616. https://doi.org/10.1016/j.ijheatmasstransfer.2020.120616
44. Wang H, Li A, Hu R, Li J (2010) Accurate stress analysis on steel box girder of long span suspension bridges based on multi-scale submodeling method. Adv Struct Eng 13(4):727–740. https://doi.org/10.1260/1369-4332.13.4.727
45. Schüßler P, Nouri N, Schulze V, Dietrich S (2023) A novel multiscale process simulation to predict the impact of intrinsic heat treatment on local microstructure gradients and bulk hardness of AISI 4140 manufactured by laser powder bed fusion. Virt Phys Prototyp 18(1). https://doi.org/10.1080/17452759.2023.2271455
46. Ferraris E, Zhang J, Van Hooreweder B (2019) Thermography based in-process monitoring of fused filament fabrication of polymeric parts. CIRP Ann 68(1):213–216. https://doi.org/10.1016/j.cirp.2019.04.123
47. Love A (1892) A treatise on the mathematical theory of elasticity vol. 1. https://hal.science/hal-01307751
48. Baehr HD, Stephan K (2011) Heat and Mass Transfer. Springer, Berlin, Heidelberg
49. BASF 3D printing solutions BV (2019) Technical Data Sheet - Ultrafuse PLA. Technical report
50. Baran EH, Yildirim Erbil H (2019) Surface modification of 3d printed PLA objects by fused deposition modeling: a review. Colloid Interface 3(2). https://doi.org/10.3390/colloids3020043
51. Elkholy A, Rouby M, Kempers R (2019) Characterization of the anisotropic thermal conductivity of additively manufactured components by fused filament fabrication. Prog Add Manuf 4(4):497–515. https://doi.org/10.1007/s40964-019-00098-2
52. Brenken B (2017) Extrusion deposition additive manufacturing of fiber reinforced semi-crystalline polymers. PhD thesis, Purdue University
53. Knirsch J, Frölich F, Hof L, Wittemann F, Kärger L (2024) pyGCodeDecode: A Python package for time-accurate GCode simulation in material extrusion processes. J Open Sourc Softw 9(99):6465. https://doi.org/10.21105/joss.06465
54. Gkertzos P, Kotzakolios A, Mantzouranis G, Kostopoulos V (2024) Nozzle temperature calibration in 3D printing. Int J Interact Des Manuf 18(2):879–899. https://doi.org/10.1007/s12008-023-01681-2
55. Tang CL, Seeger S, Röllig M (2023) Improving the comparability of FFF-3D printing emission data by adjustment of the set extruder temperature. Atmospheric Environment: X. 18(February). https://doi.org/10.1016/j.aeaoa.2023.100217